

DEVELOPMENT OF NEXT GENERATION HUMAN FE MODEL CAPABLE OF ORGAN INJURY PREDICTION

Kenji Shigeta
Yuichi Kitagawa
Tsuyoshi Yasuki

Toyota Motor Corporation
Japan
Paper Number 09-0111

ABSTRACT

Although internal organ injury in car crashes occurs at a relatively lower frequency compared to bone fracture, it tends to be ranked higher in terms of injury severity. A generalized injury risk can be assessed in car crash tests by evaluating abdominal force and viscous criterion (VC) using a crash test dummy, but the injury risk to each organ cannot be estimated with current dummies due to a lack of parts representing the internal organs. Recently, human body modeling research has been conducted introducing organ parts. It is still a challenge to simulate the impact behavior of organ parts and their injury, based on an understanding of the differences in structure and material properties among the organs.

In this study, a next generation human body FE model has been developed to predict internal organ injury. The model represents the geometry of organ parts, their location in a living human body and their connections to surrounding tissues. The features of each organ part were taken into account in modeling, so that compressive material was assumed for hollow organs while incompressive material was applied to solid organs. Besides the major organ parts, other soft tissues such as membranes and fatty tissues were also incorporated in order to simulate relative motions among organs. The entire model was examined comparing its mechanical response to that in the literature. The study confirmed that the force-deformation response of the torso against anterior loading showed a good correlation with that of tested subjects.

INTRODUCTION

Computer simulation has attracted attention in recent years as a way of predicting occupant behavior and injury criteria in vehicle collisions. In fact, research and development efforts in this field date back to the 1960s. The most common modeling method in this period, called multibody simulation, recreated vehicle occupants using rigid body elements with links (McHenry, 1963) [1]. In a multibody model, major body parts such as the head, torso, and extremities are expressed by ellipsoids, with joints defined from among them. A multibody model could

simulate impact behavior of a human body by adjusting the dimensions, mass, and inertia moment of the ellipsoids to those of the relevant body parts, and setting the rotational direction and angle of each joint with the same restrictions as human joints. It is also possible to predict mechanical response of the occupant after contact with interior parts or restraint devices by replacing the rigid ellipsoids with deformable elements. Other benefits of using multibody models in impact behavior simulations include short calculation times and simple parameter studies. However, such models are not well suited for recreating injuries such as bone fracture or soft tissue damage. In contrast, finite element (FE) models began to be used for analyzing vehicle body deformation in the 1980s. By representing structures of vehicle body panels in a FE model, it became possible to simulate deformation modes and force responses accurately. Moreover, it was also possible to predict whether metal sheets would rupture under given impact conditions by assuming the stress-strain property up to the rupture point. Despite the fact that FE simulation generally requires longer calculation times than multibody simulation, research using human FE models is an advanced method of predicting impact behavior and mechanical response. The development of human FE models started with component models, such as of the head or thorax. Such models are generated based on commercial databases of human anatomy and anatomical or sectional drawings of the body, and their material properties are input based on the mechanical properties of body tissues reported in the literature. The validity of a completed model can be verified by comparing impact response with that of post mortem human subjects (PMHS). FE models of the entire body have been built by combining component models from the head to the lower extremities. Several such models have already been developed, as reported by Choi et al. (1999) [2], Iwamoto et al. (2002) [3], Vezin et al. (2005) [4], and Ruan et al. (2003) [5].

One of these models is the Total Human Model for Safety (THUMS), which was jointly developed by Toyota Motor Corporation and Toyota Central R & D Labs., Inc., and has been used in a number of published studies attempting to reproduce injuries in vehicle collisions. THUMS includes a standing

pedestrian model and a sitting model of a vehicle occupant, both of which simulate an adult male of average physique. Iwamoto et al. (2002) used THUMS to simulate an actual traffic accident scenario (a vehicle colliding with a utility pole) and reproduced the injuries suffered by the occupants. Kitagawa et al. (2005) [6] used a human FE model to predict occupant behavior in a frontal collision to study knee joint deformation when the knees strike the instrument panel and the effect of airbags in helping to reduce such deformation. Hayashi et al. (2006) [7] and Kuwahara et al. (2008) [8] simulated vehicle side impact collisions to investigate the mechanism of rib fractures and the force-reduction effect of side airbags. In addition, Kitagawa et al. (2006 [9], 2007 [10], and 2008 [11]) simulated low-velocity rear-end collisions to analyze occupant head and cervical behavior and examine the mechanism of cervical whiplash injury. Yasuki et al. (2005) [12] also used a human FE model to predict pedestrian behavior in a vehicle collision and compare the results with the impact behavior of the TRL impactor used in lower extremity injury assessment tests.

Since injuries to the brain and internal organs generally tend to be more severe than bone fractures or ligament rupture, attempts have also been made to reproduce such injuries using human FE models. Tamura et al. (2006) [13] simulated vehicle collisions using a pedestrian model featuring a brain. This study indicated a high level of strain within the brain immediately before and directly after impact between the pedestrian's head and the vehicle's hood. In contrast, although several case studies have attempted to reproduce injuries by simulating impactor tests on PMHS, relatively few have attempted to predict organ injury under conditions equivalent to a vehicle collision. Hayashi et al. (2008) [14] demonstrated that internal lung pressure on the side facing the impact increases due to contact between the upper arm of a vehicle occupant and the side of the thorax in a side impact collision. This is a valuable piece of research that discusses internal organ injury risk under vehicle collision conditions, but it does not provide a quantifiable assessment of injury occurrence. Organs in the thoracic and abdominal areas tend to suffer greater deformation in an impact than the brain, which is encased in a highly rigid skull. However, it is not easy to accurately reproduce the mechanical response of internal organs, which are much softer than the skeleton or ligaments, or to predict their injury criteria. This research developed the next generation of the human FE model THUMS (THUMS ver.4.0). Featuring both standing and seated postures, THUMS ver.4.0 simulates the internal organ structures within the torso in detail. High-resolution CT scans were used to digitize the interior of the body and generate

precise geometrical data for the internal organs. As a result, it was possible to accurately reproduce the layout of organs within the body and their connecting structures. Moreover, the modeling reflected the anatomical features of each organ, and by inputting data on the physical properties of organ tissue reported in the latest research, it is possible to simulate injury at a tissue level. The validity of the completed model was verified by comparing its mechanical response with impact test data from PMHS. The impact simulations with the human FE model used the finite element analysis (FEA) code LS-DYNA™.

MODEL DEVELOPMENT

Torso Model

To predict organ injury accurately in a vehicle impact, it is necessary to simulate the structure inside the torso in detail. The developed model not only reproduces the geometry of the individual organs within the torso, but also their layout and connecting structures.

Acquisition of Anatomical Data - The internal torso structure was digitized in cooperation with the University of Michigan, which holds large quantities of data obtained using high-resolution CT scans. The CT scan measurement was performed for medical purposes and permission to use the data as a reference for developing the human FE model was obtained from the Michigan Institutional Review Board. Data groups of males in their 30s of average height and weight close to that of a 50th percentile American male (AM50: 175 cm, 77 kg) were extracted from the available data (approximately 558,000 people), and checked to eliminate samples with visible pathological abnormalities in the torso. The data of a 39-year old male with a height of 173 cm, a weight of 77.3 kg, and a BMI of 25.8 was selected. The CT scan data was measured at a pitch of 0.625 mm for the thorax, and 5 mm for the abdomen. Figure 1 shows images of the skin, skeleton, and soft tissue included in the scanned data. The scanned data was converted into Standard Triangulated Language (STL) format polygons for each body and tissue part using the 3D image conversion tool MIMICS™. The skeletal structure was identified by applying a masking process to the CT scan images at a threshold value of 130 Hounsfield units (HU). The soft tissue was identified by a conversion process using a different HU level for each organ. The process was performed while verifying any partial omissions in the created polygon data. The following organs were converted into polygon data: heart, lungs, liver, kidneys, spleen, pancreas, gall bladder, bladder, esophagus, stomach,

duodenum, small intestine, and large intestine. However, due to the thinness of its walls, it was difficult to generate polygon data that reproduced the path of the small intestine. Compression of the abdomen not only causes compressive deformation in the small intestine itself, but also generates movement together with the neighboring area. Therefore, this model does not reproduce the exact path of the small intestine, but instead expresses the whole of the small intestine as a single element. In contrast, the paths of each artery and vein, and their connections to each organ were reproduced in polygon data. The end diameters of the blood vessels connected to each organ are expressed to a detail of approximately 5 mm. In addition, geometry for membranes surrounding the organs, such as the diaphragm, pleurae, peritoneum, and fascia, was also extracted. Thus, organs such as the pancreas, kidneys, bladder, small intestine, and large intestine are expressed as shapes included within the peritoneum. Separate polygon data was also generated for visceral fat. Subcutaneous fat, muscle, and the microscopic blood vessels between the skin and skeleton and between the skin and peritoneum were treated as belonging to the same group. The spinal cord was expressed within the spinal canal as a separate polygon data group from the vertebral body.

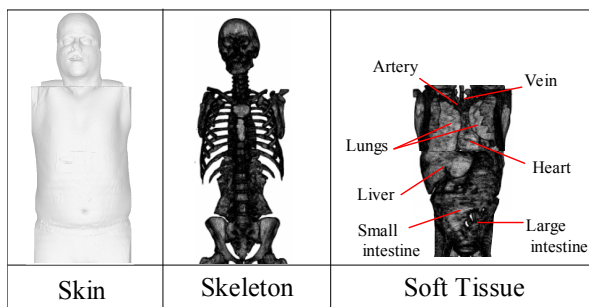


Figure 1. CT scan data.

Creation of FE Model - Surfaces were created by feeding the polygon data into the HyperMesh™ mesh generator. Geometrical features with unnatural disconnections in the generated surfaces (such as bends or projections) were repaired in reference to anatomical drawings and the like. Interference between surfaces created for separate parts (particularly adjacent curved surfaces and so on) was handled by receding the surface geometry of the interfering portion without disturbing the shape of the parts. Guidelines were established before generating the FE mesh. The mesh density was adjusted so that the element length became 3 to 5 mm, which divided the sternum, a relatively small bony part in the thorax, into two sections in the anterior-posterior direction. In addition, the aorta, also a small organ part, was divided into eight

elements in the circumference direction. The reference values for the quality of element geometry were set as follows: warpage = 50 degrees or less, aspect ratio = 5 or less, skew = 60 degrees or less, Jacobian = 0.3 or more. Solid elements were used wherever possible for FE mesh generation. However, since many cortical bones within the torso skeletal structure have a thickness of around 1 mm, these bones were modeled using shell elements and cancellous bones with solid elements. For soft tissue, solid organs and thick hollow tissue were modeled with solid elements, and thin tissue such as blood vessels and membranes were modeled with shell elements. In addition, cortical bones and soft tissue with little curvature were divided into quadrilateral shell elements and hexahedral solid elements. The appropriate hourglass control logic was applied to each type of element, using full integration for the shell elements and 1-point integration for solid elements. In addition, skin and subcutaneous fat adjacent to joints were modeled using quadrilateral elements to facilitate FE mesh regeneration after changes in posture.

Nodes at boundary surfaces between connective tissue were shared. For example, each of the following tissues are defined as separate parts, but include elements with shared nodes at their adjacent boundary surfaces: cortical and cancellous bones; rib cartilage and costal bones; the aorta/vena cava and the heart/lungs; and the digestive system (stomach/duodenum/small and large intestines) from the esophagus. Parts of various organs join with other tissue, for example, the superior portion of the liver joins with the diaphragm, and a portion of the rear of the large intestine joins with the peritoneum. These joints were also expressed with shared nodes at the corresponding parts. Other boundary surfaces, for example between different organs or between non-connecting organs and membranes, were defined to perform contact processing. It was assumed that no friction occurs between contact surfaces. Figure 2 shows the skeletal structure and internal organs of the torso model.

Skeletal parts were assumed to have elasto-plastic properties capable of expressing tissue injury. Membrane material was applied to ligaments and organ membranes, whereas incompressible material was assumed for the solid parts of organs. Compressive material was assumed for hollow organs such as the small and large intestines. The structure of the lungs includes air within the pulmonary alveoli. Membrane material was applied to the organ surface and their interior portions were expressed with elastic material simulating gas. Blood vessels were given the same structure. The physical properties input into each material model were selected from data obtained by Yamada (1970) [15] and Abe et al. (1996) [16].



Figure 2. Skeletal structure and internal organs of torso model.

Head Model

THUMS ver.3.0 was used for the head model (Figure 3). This model was developed by Kimpara et al. (2006) [17] and its accuracy was validated against mechanical response results of impact tests in the literature. The elements in the FE mesh have a length of approximately 10 mm for the epidermis but 3 to 7 mm for the brain part that is essential for injury prediction, and matches well with the developed torso model. The merging positions of the models are as follows: the lower extremity of the cervix for the skin and subcutaneous fat, and the upper extremity of the cervix for the spine and spinal cord. The spinal cord is provided within the spinal canal using solid elements simulating the surrounding cerebrospinal fluid (CSF) and fatty layer. Its surface contacts that of the vertebral body without sharing nodes. Material properties equivalent to water are assumed for the CSF part. The cervical muscles are modeled in 1D elements in the same way as in THUMS ver.3.0, and recreate only resistance force when forcibly elongated. Table 1 lists the physical properties of the head model.

Extremity Models

Excluding the pelvis, the FE meshes of the extremities were modeled in reference to ViewPoint™ geometrical data (Figure 4). The element division guidelines were the same as for the torso model. Since the extremity models are mostly used for assessing bone fractures, each leg model used solid elements to express the cortical bones as well as the femur, patella, tibia, and fibula (Figure 5).

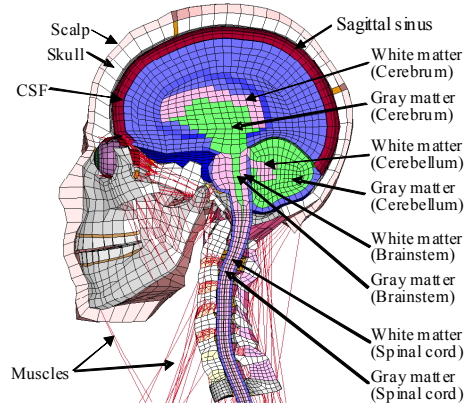


Figure 3. Head model (THUMS ver. 3.0).

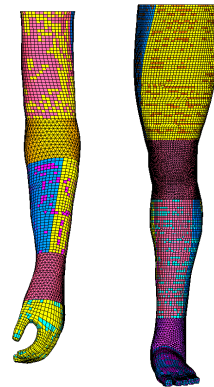


Figure 4. Outline of extremity models.

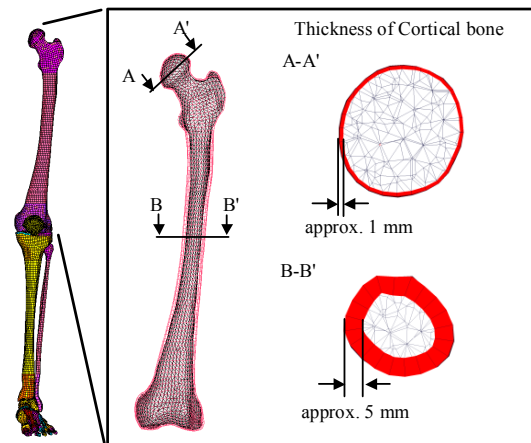


Figure 5. Section of bone along length of leg.

Knee joint ligament injury risk is estimated to evaluate pedestrian protection performance. The cruciform and collateral ligaments were modeled using solid elements (Figure 6). Solid elements were also used for the tendon of the quadriceps femoris muscle, the patellar ligaments, and the Achilles

tendon. The integration points and material properties of the elements were set along the same lines as the torso model. Table 1 also lists the material properties defined in the extremity models. The extremities contain abundant musculature, which has a major effect on behavior and mechanical response in an impact. This study divided the muscles of the extremities into the major muscle groups. The upper extremity and tibia portions were divided into flexing and extending muscle groups. Adductor muscles were also provided for the femur portion in addition to the above two groups. The dividing positions for the muscle groups were determined based on anatomical reference books and visual data from the Visible Human Project. Shared nodes were provided for the parts at the boundaries between each muscle group and the skeletal structure, and between the muscles groups and the skin. Contact processing was applied between the muscle groups so that compression causes both movement and sectional deformation of each group. A friction coefficient of zero was assumed for the surface of the fascia. The extremity models were joined to the torso model at the shoulder and hip joints. The merging portions were modeled using shell elements equivalent to joint ligaments. The humerus was connected to the scapula and clavicle, and the femur was connected to the pelvis. The articular capsules were also modeled using shell elements. The FE mesh for the skin and muscles of the torso and extremity models was made consistent.

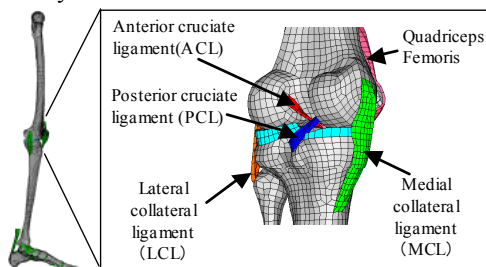


Figure 6. Knee joint ligaments.

Whole Body Models

The whole body models were assembled by fusing the torso, head, and extremity models. Since the CT scan torso geometry data was obtained while the subject was recumbent on the device looking upward, the standing model was created first. This model simulates a person standing in an upright position with their legs open at shoulder width. Both arms are hanging straight down to the sides of the torso. The

seated model, simulating a vehicle occupant, was then created based on the standing model. The model was modified to position the lumbar vertebrae in a natural seating posture. The arms and legs of the seated model are both slightly extended in front of the torso. Figure 7 shows an outline of both models. Each contains approximately 630,000 nodes and 1.8 million elements. The model has a height of 178.6 cm and a weight of 63.0 kg, which is close to the person used as the basis for the torso model.

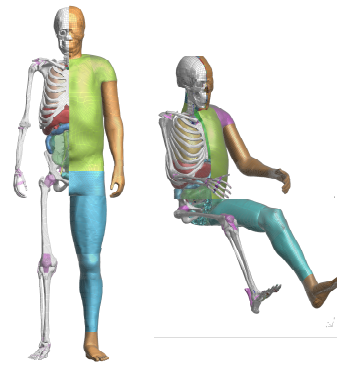


Figure 7. Outline of whole body models (standing and seated).

MODEL VALIDATION

The validity of the completed model was verified by comparing its mechanical response with the results of PMHS impact tests in the literature [20]-[25]. For verification, the conditions of the actual tests had to be reproduced using the FE model. For this reason, the selected test cases were those with detailed information on the impact conditions such as impactor geometry and velocity and the PMHS injury results. In addition, the posture of the assembled standing model was modified in accordance with the test conditions. Table 2 lists the literature data used for the validation. It is common for thoracic and abdominal impact tests to use an impactor, but the results of tests involving the application of a belt-shaped compressive force were also used to simulate a vehicle occupant wearing a seatbelt. Since the extremity models are mostly used to evaluate bone fracture and ligament injury, 3-point bending tests were selected for the bones in the upper and lower extremities and impactor tests were selected for the knees. The head and neck models have already been verified by Kimpara et al. (2006), but the literature data for these cases is also included in Table 2 for reference.

Table 1. Material characteristics of model body parts and tissues

			Density (kg/m ³)	Young's modulus E (MPa)	Poisson ratio	Yield stress (MPa)	Ultimate stress (MPa)	Reference		
Bone	Skull	Frontal bone	Cortical	2,120	11,000	0.22	48	Yamada (1970) Wood (1971) Abe et al. (1996)		
			Trabecular	1,000	100	0.22	0.35			
		Parietal, temporal,	Cortical	2,120	11,000	0.22	48			
			Trabecular	1,000	1,000	0.22	4.8			
		Facial bones	Cortical	2,120	11,000	0.22	48			
			Trabecular	1,000	200	0.22	0.7			
	Skull suture		2,120	13,000	0.22	12	Naruse (1993)			
	Vertebrae		Cortical	2,000	12,000	0.3	100	Yamada(1970)		
			Trabecular	1,000	1,000	0.3	8.3	Abe et al.(1996)		
			Cortical	2,000	9,860	0.3	66.7	Kimpara (2005)		
	Thorax	Rib / Sternum	Trabecular	1,000	40	0.45	1.8	Yamada(1970)		
			Costal	1,000	49	0.4	4.9	Abe et al.(1996)		
	Upper extremity		Cortical	2,000	11,000	0.3	110			
			Trabecular	1,000	1,100	0.3	7.7			
			Cortical		18,500	0.3			146	
	Lower extremity	Fibula	Trabecular		145.6	0.45		30.6	Yamada (1970)	
			Cortical		15,000	0.3		140		
		Talus	Trabecular		145.6	0.45		30.6		
			Cortical		15,000	0.3		140		
		Calcaneus	Trabecular		145.6	0.45		30.6		
			Cortical		17,000	0.3		150		
		Femur	Trabecular		145.6	0.45		30.6		Iwamoto et al. (2005)
			Cortical		18,000	0.3		150		
		Tibia	Trabecular		145.6	0.45		30.6		
Soft tissue	Diaphragm		1,000	2	0.4	2	Shah et al. (2001)			
		Cervical	2,000	1	0.4	2				
	Pleural, Mediastinum, Peritoneum, Fascia		1,000	13	0.4	1				
	Skin		900	31.5	0.45	0.1		Shah et al. (2001)		
	Aorta		4,000	4	0.4	3				
	Ligaments		1,100	9 - 100	0.22	1 - 3		Yamada(1970) Abe et al.(1996)		
	Fat		900	0.5				Lee and Yang (2001)		
	Muscle		900	0.5						
Intercostal		1,000	1	0.3		Yamada (1970)				
Brain	CSF		1,000	1.60E-04	0.49		Galford and McElhaney (1970)			
	Sagittal sinus		1,000	1	0.49					
	Pia mater		1,000	1.1	0.4	0.4	McElhaney et al.(1973)			
	Arachnoid		1,000	1.1	0.4	0.4				
	Meninx		1,000	31.5	0.45	0.2	Al-Bsharat et al.(1999)			
	Tentorium		1,133	31.5	0.45	1	Willinger(2003)			
	Dura mater		1,133	31.5	0.45	1	Zhang et al.(2002)			
	Falx cerebri		1,133	31.5	0.45	1	Tokhounts et al.(2003)			
				Density (kg/m ³)	Modulus K (Mpa)	Shear Modulus G ₀ (Mpa) G _∞ (Mpa)		Reference		
	Cerebrum	White	1,000	2,160	0.0125	0.0061	Galford and McElhaney (1970)			
		Gray	1,000	2,190	0.010	0.005				
	Cerebellum	White	1,000	2,160	0.0125	0.0061	McElhaney et al.(1973)			
		Gray	1,000	2,190	0.010	0.005	Nakamichi et al.(2001)			
	Brainstem	White	1,000	2,190	0.023	0.0045	Zhang et al.(2002)			
Gray		1,000	2,190	0.010	0.005	Tokhounts et al.(2003)				
Neck	Cervical bone	Cortical	2,000	12,000	0.3	100	Yamada(1970)			
		Trabecular	1,000	1,000	0.3	8.3	Abe et al.(1996)			
	Cervical dura mater	Anterior	1,100	44.1	0.3	0.33	Yamada(1970)			
		Posterior	1,100	43.35	0.3	0.68				
	Anterior Longitudinal Ligame					5.65	Yoganandan et al. (1989a and 1998)			
	Posterior Longitudinal Ligame			40.9		4.54				
	Interspinous Ligament(ISL)			4.9		1.28				
	Ligament Flavum(LF)			3.1		1.26				
Transvers Ligament(TL)			3.1		1.26					
Capsular Ligament(CL)			5		2.84					
Internal organ				Property data				Preference		
				Nominal strain [%]						
				10	20	30	50			
	Heart			5.4	12.4	28	374.9		Yamada (1970)	
	Lung			7.9	14.1	20.1	31.7		Hayamizu (2003)	
	Liver			2.5	14.7	58.9	380.2		Tamura (2002)	
	Spleen			1.5	2.5	3.7	9.8		Ishikawa (2000)	
	Kidney			4.9	36.3	134.4			Yamada (1970)	
	Small intestine			17.7	38.2	94.1	778.6			
	Large intestine			16.3	29.4	40.9	163.4			
Blood vessel			14.9	29.7	66.9	193.2				
Stomach			4.5	12.7	28.1	93.2				

Table 2. PMHS test data used in validation

	Test condition	Reference
Thorax	Thoracic frontal impact	Kroell et al. (1974)
	Thoracic dynamic belt compression	Cesari et al. (1990)
Abdomen	Abdomen frontal impact	Cavanaugh et al. (1986)
	Abdomen dynamic belt compression	Foster et al. (2006)
Upper extremities	Humerus static three point bending	Kemper et al. (2005)
	Humerus dynamic compression	
Lower extremities	Femur static three point bending	Yamada et al. (1970)
	Knee joint lateral loading	Kajzer et al. (1997, 1999)
Head and brain	Head impact	Nahum et al. (1977)
		Troseille et al. (1992) Hardy et al. (2001)
Head and neck	Neck flexion and cervical axial compression	Pintar et al. (1995) Thunnissen et al. (1995)

Cases of described injury conditions in the literature were compared with prediction results using the FE model. The FE model predicted injury based on the reference values shown in Table 3. Bone fracture was assumed to have occurred when the strain of the elements included in a cortical bone exceeded 3% [24]. Evaluation indices and reference values were assumed for each internal organ. Pulmonary contusion, i.e., injury to the alveolar tissue when the pressure inside the lungs increases due to blunt external force, is the most frequent lung injury mode. For this reason, a pressure index was applied to the elements inside the lungs. Karl et al. (1958) reported that there is a risk of alveolar tissue injury when the internal pressure of the lungs exceeds ± 10 kPa [25]. Strain indices were applied to the other organs. A typical heart injury mode is myocardial laceration. Although the rupture threshold of the myocardial muscle differs depending on the direction of force to the muscle fiber, Yamada (1970) states that tissue damage begins to occur with strain of 30% or above. Melvin et al. (1973) reported that the strain threshold for liver and kidney injury is approximately 30%, depending on the compression velocity. The reference value for the spleen is assumed to be 30%, the same as for the liver. Yamada (1970) also states that the rupture strain for the intestines is approximately 120%, and approximately 100% for thoracic and abdominal blood vessels. It should be noted, however, that the validity of these indices and reference values requires further investigation and verification. This study does not debate the absolute accuracy of the organ pressures or strain levels predicted by the FE model, but simply compares the organ injuries predicted by the FE model with the conditions of PMHS injury assuming the reference values for injury criteria in Table 3.

Table 3. Reference values for injury criteria

		Index	Threshold	Reference
Bone		Strain	3.06%	Kemper et al.(2005)
Internal Organ	Heart	Strain	30%	Yamada et al.(1970)
	Lung	Pressure	± 10 kPa	Karl et al.(1958)
	Liver	Strain	30%	Melvin et al. (1973)
	Spleen	Strain	30%	-
	Intestine	Strain	120%	Yamada et al. (1970)
	Blood vessel	Strain	100%	

Verification of Thorax Model

Thoracic Impactor Response - Figure 8 shows the thoracic impactor test performed by Kroell et al. (1971, 1974). In this test, cylindrical impactors simulating a steering wheel hub (diameter: 152 mm, mass: 7.92 to 23.6 kg) were collided with the anterior surface of the thorax of a PMHS at an initial velocity of 6.3 to 14 m/s. Each test was synchronized on high-speed film and the displacement and acceleration of the impactor were measured to calculate force-deflection curves. This impactor test was performed on 38 PMHS to create a force response corridor for each impactor mass and initial velocity. Verification of the force response of the FE model referred to a corridor created under typical conditions (mass: 23.1 kg, initial velocity: 7.2 m/s). The state of injury after each test was reported for each PMHS. Verification of FE model injury prediction used 20 cases close to the force conditions (mass: 19.5 to 23.6 kg, initial velocity: 6.3 to 10.19 m/s). The posture of the PMHS in the tests is not described in the literature in detail but the FE model adopted an upright seated posture on the test device with both arms forward of the body, based on assumptions from photographs and images in the reports. The impactor force was output as a contact load between the impactor head and the anterior surface of the thorax. Impactor displacement was calculated from model node displacement, and thoracic deflection was calculated from changes in the distance between nodes on the anterior and posterior surfaces of the thorax.

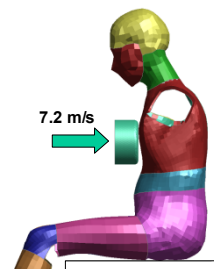


Figure 8. Thoracic impactor test.

Figure 9 shows the observed state of the thoracic geometry after impactor contact. The sectional diagrams are viewed from the left side of the body's median sagittal plane, and show thoracic deflection

of 0 mm, 15 mm, 30 mm, and 78 mm. In this case, maximum thoracic deflection was 78 mm. Up to an thoracic deflection of 15 mm, the skin and subcutaneous tissue (fat and muscle) were compressed. Deformation of the inferior portion of the sternum and the rib cartilage began at an thoracic deflection of 30 mm, initiating compression of the underlying heart and lungs. Rib deformation had progressed at an thoracic deflection of 78 mm, increasing the compressive deformation on the heart and lungs. After this point, since the posterior surface of the torso was not supported in the test, the spine at the height of the impactor displaced to the rear and the whole spine curved. Figure 10 shows the superior view of the horizontal section of the thorax at the height of the impactor center. It compares the states at thoracic deflection of 0 mm (initial state) and 78 mm. This section includes the sternum, ribs, spine, heart, and lungs. The contact area of the impactor includes the heart and a part of the lungs. The sectional deformation at an thoracic deflection of 78 mm shows that the heart was compressed in the anterior-posterior (AP) direction between the sternum and the spine, and that the heart elongated in the lateral direction. Additionally, the anterior surface of the thorax including the sternum and the ribs deformed into a flat shape along the contact surface with the impactor. The anterior portion of the lungs then deformed accordingly.

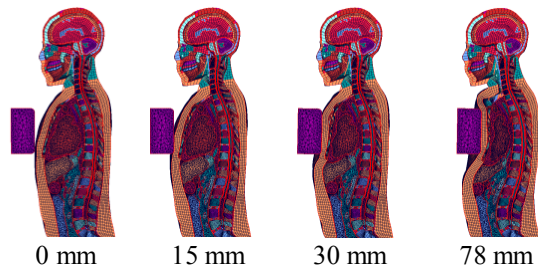


Figure 9. Thoracic deformation after impactor contact.

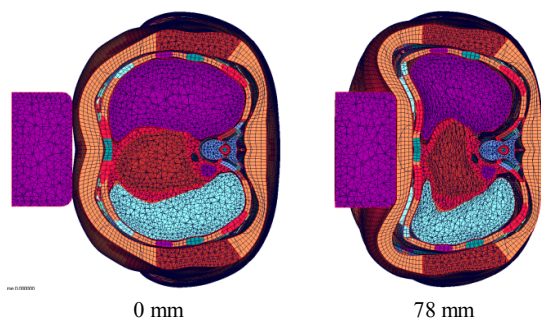


Figure 10. Sectional deformation of thorax (at height of impactor center).

Figure 11 compares the thoracic force response of the PMHS and FE model, with thoracic deflection on the horizontal axis and impactor force on the vertical axis. The force response of the PMHS is shown in the grey corridor and that of the FE model by the black solid line. Force initially peaked in both the PMHS and FE model at a thoracic deflection of 10 to 20 mm, before reaching a maximum peak at approximately 80 mm. The initial peak force with the PMHS was in a range from 2.5 to 4 kN, and the FE model recorded 3.5 kN. The maximum peak force with the PMHS was in the range from 3 to 4.5 kN, and was 4.5 for the FE model. Therefore, the peak force calculated by the FE model roughly corresponded to the range of the PMHS, but its force response curve partially fell outside the PMHS corridor. At around 20 mm, after the first peak force calculated by the FE model, the force fell to 1.5 kN, clearly below the PMHS corridor. However, several of the force response curves described in the literature also describe the force decreasing to a range of 1.5 to 3 kN after the initial peak. Thus, the 1.5 kN calculated by the FE model here was judged to be within the appropriate range.

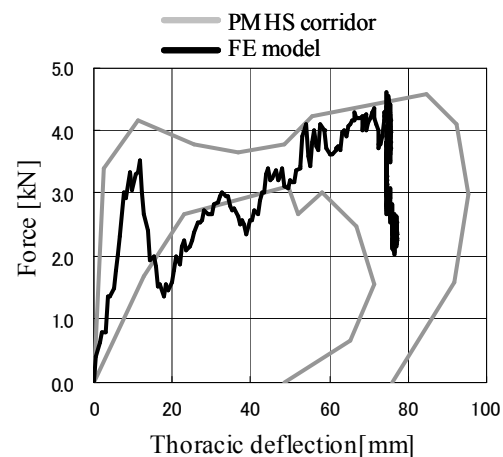


Figure 11. Comparison of thoracic force-deflection response.

Table 4 compares PMHS autopsy results and FE model predictions with respect to injury to the skeletal structure and the organs in the thorax. Kroell at al. (1971, 1974) reported that 18 of the 20 PMHS cases relevant to the model verification in this study incurred some kind of injury. All of these injury cases involved sternum or rib fracture, and 15 suffered soft tissue injury. Rib fractures occurred in an average of 11 locations from the first to the seventh ribs. With respect to organ injury, cases of heart and liver injury were most frequent (5), followed by the lungs (4). Cases of membrane injury were also frequent (9). The FE model predicted that cortical bones in the

sternum and ribs would have exceeded the 3% reference value for fracture strain in 8 locations. Two of these were located at the inferior portion of the sternum, and the other six occurred at either the left or right ribs. Figure 12 shows the corresponding locations. Figure 13 shows the state of occurrence for maximum principal strain and pressure in the FE model heart. Strain exceeded 0.3 in the heart and liver. Strain in the liver concentrated in the position

at the center of the body corresponding with the contact position of the impactor. High levels of strain were also detected in an area of the stomach, but this was below the reference value of 1.2. Strain did not exceed the reference value in any of the other organs. Additionally, lung pressure exceeded 10 kPa. The state of organ injuries predicted by the FE model correlated well with the PMHS autopsy results.

Table 4. Injury cases and predicted results

Subject		Impact Condition		Bony Fractures		Soft Tissue Injuries				
Age	Gender	Mass	Velocity	Sternum	Ribs	Heart	Lung	Liver	Aorta	Others
60	F	19.5	6.3	0	11					
67	F	22.9	7.2	2	22		Y			
81	M	22.9	7.4	0	21	Y				
76	F	22.9	7.2	2	7	Y			Y	
80	M	23.6	6.9	0	13		Y			
78	M	23.6	6.7	2	14					Y
19	M	23.6	6.7	1	0					
29	M	23.6	6.7	0	0					
45	F	23.6	6.8	1	18					
72	M	23.6	6.7	0	17			Y		Y
58	F	19.5	7.7	0	23		Y			Y
65	M	22.9	9.7	2	M		Y	Y		Y
51	M	23.04	10.19	1	14					Y
75	M	22.86	9.92	1	20	Y				Y
64	M	18.96	8.23	0	13					Y
52	M	18.96	7.2	0	7			Y		
48	M	22.86	9.83	1	9			Y	Y	Y
46	M	19.28	7.33	0	0					
49	F	19.55	6.71	0	7	Y		Y		
46	F	19.55	9.92	0	8	Y				Y
				Average of Fractures		Numbers of Soft Tissue Injuries				
				Sternum	Ribs	Heart	Lung	Liver	Aorta	Others
				0.65	11.2	5	4	5	2	9
FE model		23.0	7.2	2	6	Y	Y	Y		

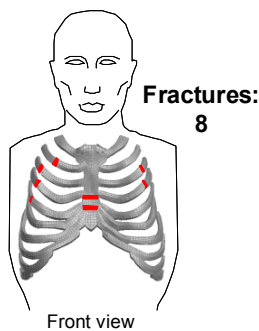


Figure 12. Bony fracture prediction in thoracic impactor test.

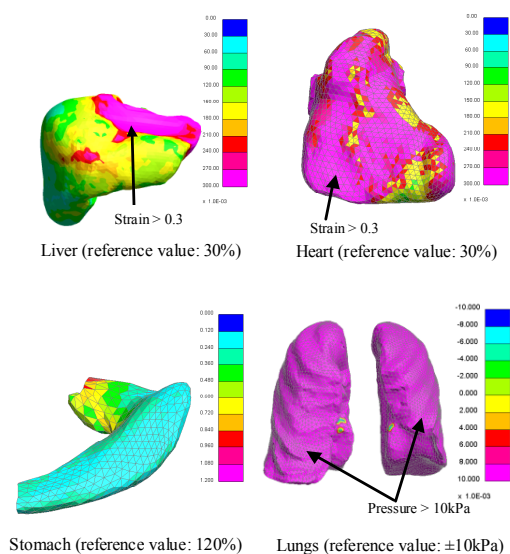


Figure 13. Strain and pressure distribution in thoracic organs (liver, heart, stomach: strain distribution; lungs: pressure distribution).

Thoracic Belt Compression Response - Figure 14 shows the thoracic belt compression test performed by Cesari et al. (1990). The test involved placing a belt-shaped impactor (width: approximately 50 mm) diagonally across the anterior surface of the thorax of a PMHS lying face upward on a test bench to simulate a seatbelt, and pulling both ends of the belt toward the posterior surface of the torso. The ends of the belt were connected by wires to a pressure receiver, and pulled the belt dynamically to simulate impactor contact. Displacement was recorded at multiple points on the thorax and measured on bar-shaped deflection meters suspended from the top of the test bench. The test was performed using 13 PMHS, and their injuries were recorded in post-test autopsies. The FE model was also placed face upward on a rigid flat plane simulating the test bench. The geometry of the spine was adjusted to that of the table by applying gravitational acceleration. The time history of the amount of belt pulling force in the PMHS test was input into the FE model belt ends. An impactor mass of 22.4 kg and an initial velocity of 7.78 m/s were selected from the various test conditions. The displacement measurement points were selected by referring to diagrams showing the test conditions. If the belt moved during compression, the node closest to the initial position on the plane was re-selected. Injury was predicted based on the reference values in Table 3.

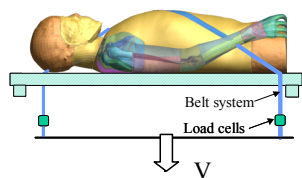


Figure 14. Thoracic belt compression test.

Figure 15 shows sectional views of thoracic deformation under belt compression from the left side of the median sagittal plane. The deformation is shown with thoracic deflection of 0 mm (0 ms), 20 mm (14 ms), and 70 mm (26 ms). As with the impactor test, compressive deformation of the subcutaneous tissue occurred before rib cage deformation. At a thoracic deflection of 30 mm, the sternum was pushed in the posterior direction, causing compressive deformation of the heart and lungs. When this occurred, the heart elongated in the inferior direction, also pressing the liver in the same direction. At a thoracic deflection of 70 mm, the sternum was pushed even further inward, advancing the deformation of the heart and lungs, and forcing the liver even further in the inferior direction. Since the posterior surface of the model was positioned

against a flat plate under these test conditions, little motion was generated in the spine. The rib cage and organs incurred compressive deformation only in the areas where the belt force was applied.

Figure 16 shows the superior view of the horizontal section of the thorax at the height of the sternum center. It compares the deformation at thoracic deflections of 0 mm and approximately 70 mm (maximum deflection). This section includes the sternum, ribs, spine, heart, and lungs. The belt contacted the anterior surface of the thorax close to the sternum. The sectional deformation at the maximum deflection shows that the heart was compressed in the AP direction between the sternum and the spine, and that the body elongated in the lateral direction. Maximum deformation of the anterior surface of the thorax occurred at the belt contact position close to the sternum, and the surrounding ribs deformed dragged by the sternum. Although lungs deformation was seen close to the sternum, no significant deformation occurred in any other location.

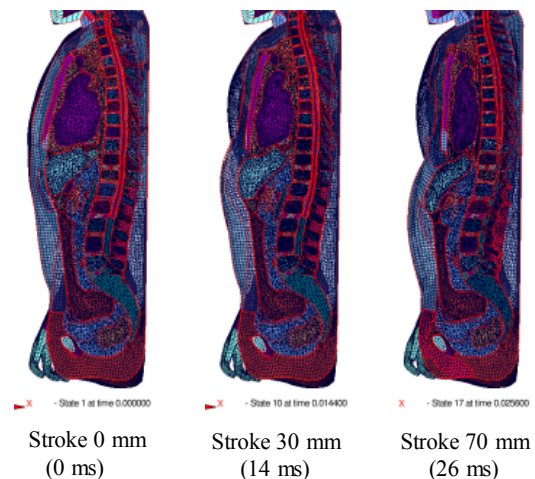


Figure 15. Thoracic belt compression behavior.

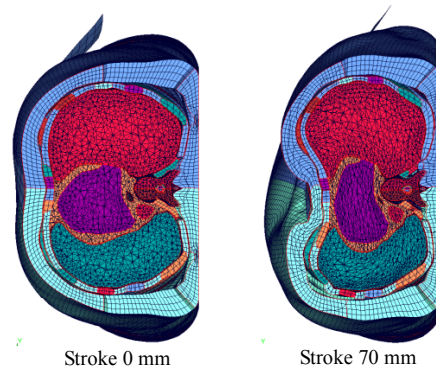


Figure 16. Sectional deformation of thorax (at height of sternum center).

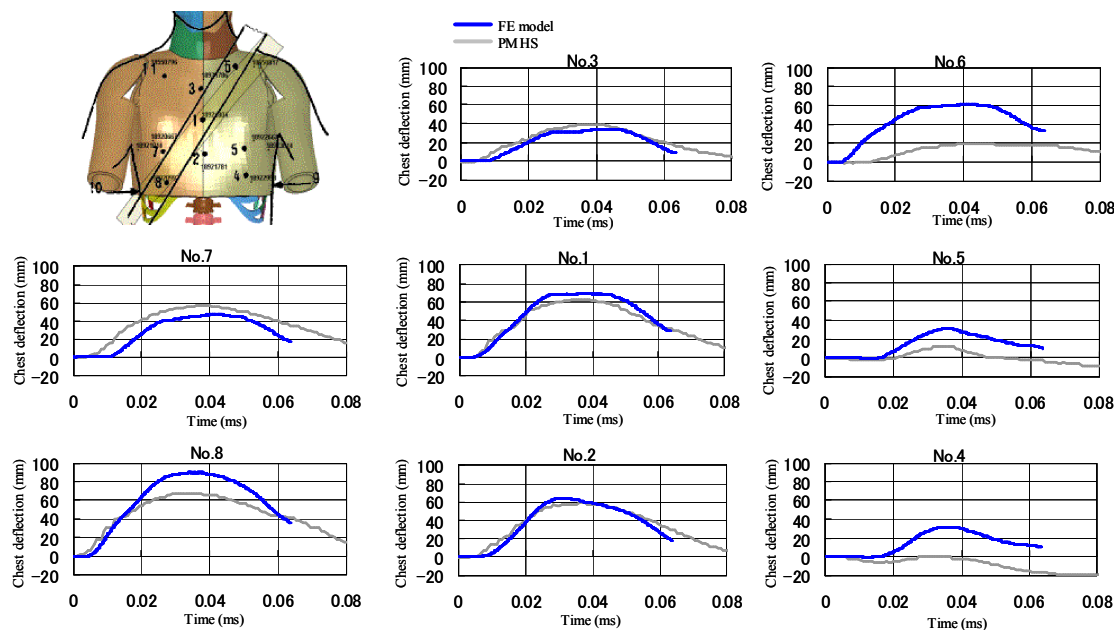


Figure 17. Displacement under thoracic belt compression.

Figure 17 shows the time history curves of displacement at each measurement point. The grey lines show the PMHS test results and the black lines show the results measured by the FE model. The same increasing trend for sternum displacement was achieved by both the PMHS and the FE model. Maximum deflection of the superior portion of the sternum was 10 mm larger with the PMHS and deflection in the center and inferior portions was 5 mm larger with the FE model. Maximum deflection measured at the rib cartilage showed a difference of 10 to 30 mm. Displacement at the left clavicle was 40 mm larger with the FE model.

Because no information on organ injury is available from the study by Cesari et al. (1990), the validity of the organ pressure and strain predicted by the FE model cannot be examined for these belt loading conditions.

Abdominal Impactor Response - Figure 18 shows the abdominal impactor test performed by Cavanaugh et al. (1986). This test impacted an aluminum bar (diameter: 25 mm, mass: 32 or 64 kg) against the abdomen of PMHS horizontally at an initial velocity of 5 to 10 m/s. The test was performed using 12 PMHS. Five of the tests used an average initial velocity of 6.1 m/s, and the remaining seven tests used an average initial velocity of 10.4 m/s. Each test recorded the abdominal deflection with respect to the impactor force, and the injury state of the PMHS was investigated after the test. Model verification referred to a force-deflection corridor created from the results of the five tests that used low initial impactor velocities. Since the posture

of the PMHS in the tests is not described in detail in the literature, an upright seated posture was assumed in the same way as the thoracic impactor test. However, both arms were positioned hanging downward. The impactor force was output as a contact load between the impactor and the anterior surface of the abdomen. Impactor displacement was calculated from model node displacement, and abdominal deflection was calculated from changes in the distance between nodes on the anterior and posterior surfaces of the abdomen.

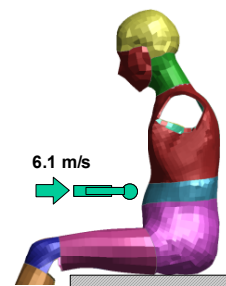


Figure 18. Outline of abdominal impactor test.

Figure 19 shows sectional views from the left side of the median sagittal plane of the FE model torso. The figure shows the states of the model at impactor strokes of 0 mm, 36 mm, 82 mm, and 100 mm. Up to 36 mm, compressive deformation was limited to the subcutaneous tissue, before subsequently spreading to the organs in the abdominal cavity such as the intestines. The compression ratio of the small intestine exceeded 90% at a stroke of 82 mm and the abdominal soft tissue impacted by the impactor

almost contacted the spine. After this point, since the posterior surface of the torso was not supported, the whole spine curved. No major changes in intestinal compression occurred in the impactor stroke range of 82 to 100 mm.

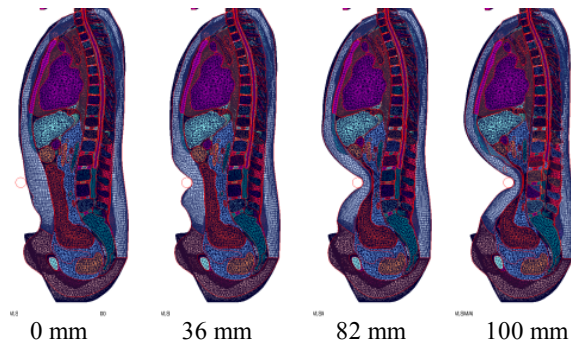


Figure 19. Abdominal impactor test behavior.

Figure 20 compares the deformation of the horizontal section of the abdomen at the height of the impactor center in its initial state and at an impactor stroke of 100 mm. The abdominal sections are viewed from the superior view and include the spine, the large intestine, the visceral fat near these organs, and the musculature at the posterior portion of the torso. The final contact range of the impactor covered the whole width of the abdomen. The sectional deformation at an impactor displacement of 100 mm shows that the anterior portion of the abdomen flattened in accordance with the shape of the impactor. The abdomen depth was compressed in the AP direction, but was elongated in the lateral direction. The small intestine was compressed in the AP direction between the subcutaneous tissue at the anterior surface of the abdomen and the spine. In contrast, compression of the large intestine was smaller and there was no major compressive deformation of the musculature at the posterior portion of the torso.

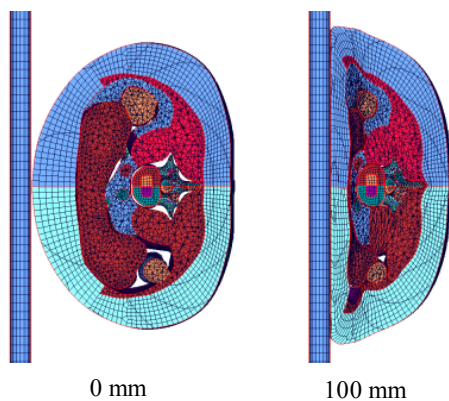


Figure 20. Sectional deformation of abdomen (at height of impactor center).

Figure 21 shows the time history curve of the impactor force with respect to its stroke. The grey lines show the force corridor calculated from the PMHS abdominal response, and the black line shows the response of the FE model. Impactor force at a stroke of 50 mm was between 0.8 and 1.9 kN with the PMHS and 1.5 kN with the FE model. In addition, at a stroke of 100 mm, the force was between 1.5 and 3 kN with the PMHS and 2.4 kN with the FE model. These results verify that the force curve of the FE model was appropriately within the PMHS corridor.

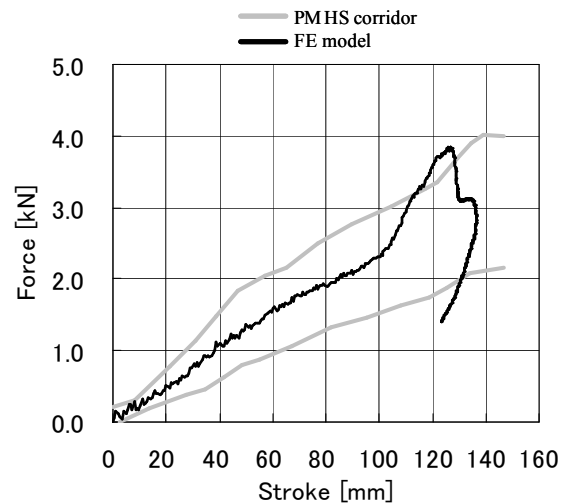


Figure 21. Abdominal impactor test F-s.

Cavanaugh et al. (1986) reported organ injury in one of the five test cases at the low initial velocity. Autopsy results show that AIS 4 liver injury occurred, but no mention is given of the small intestine. Figure 22 shows the strain distribution of the abdominal organs in the FE model. It indicates that strain in the liver exceeded the reference value of 0.3. A portion of the small intestine also exceeded the strain reference value of 1.2. The predictions of the FE model matched the test results with respect to liver injury, but close comparison was not possible due to a lack of data for other organs.

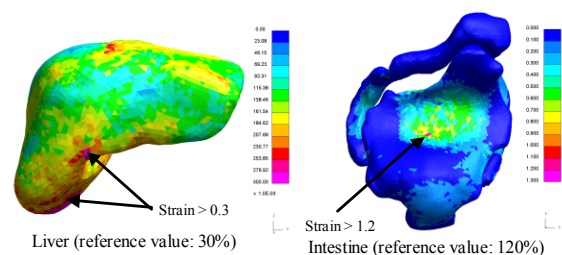


Figure 22. Strain distribution in abdominal organs.

Abdominal Belt Compression Response - Figure 23 shows the abdominal belt compression test performed by Foster et al. (2006). The test involved placing a lap belt (width: 50 mm) across the anterior surface of the abdomen of a PMHS and using a pyrotechnic pretensioner to pull the wound end toward the posterior surface of the PMHS in the horizontal direction. The posterior surface of the PMHS was supported by a rigid plate. The pretensioner had three settings for adjusting the pulling force to provide belt velocities of 4.0 to 5.4 m/s, 6.1 to 7.5 m/s, and 6.9 to 13.3 m/s. Belt force was measured by a load cell and abdominal deflection was measured by a laser deflection meter. The injuries of the PMHS were investigated after the tests. The FE model was set to reproduce the PMHS posture described in the literature, and a rigid plate was simulated at its posterior surface. Shell elements to simulate the belt were fitted to the torso around the abdomen, and the belt was pulled toward the posterior surface of the model. The comparison used the case with a belt pulling velocity of 6.9 m/s to recreate the time history of the pulling force of the belt end. Belt force was output from the sectional force of the shell elements, and abdominal deflection was calculated from changes in the distance between nodes on the anterior and posterior surfaces of the abdomen.

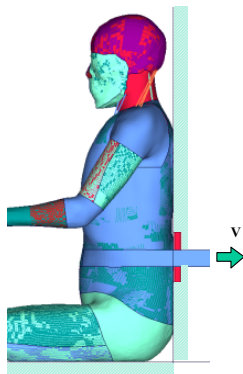


Figure 23. Outline of abdominal belt compression test.

Figure 24 shows sectional views from the left side of the median sagittal plane of the FE model torso. Abdominal deflection is shown at impactor strokes of 0 mm, 30 mm, 60 mm, and 120 mm. Up to 30 mm, compressive deformation was limited to the subcutaneous tissue, before subsequently spreading to the soft tissue in the abdominal cavity such as the small intestine. Compressive deformation of the small intestine progressed at an impactor stroke of 60 mm, and at 120 mm, the compression ratio exceeded 90%.

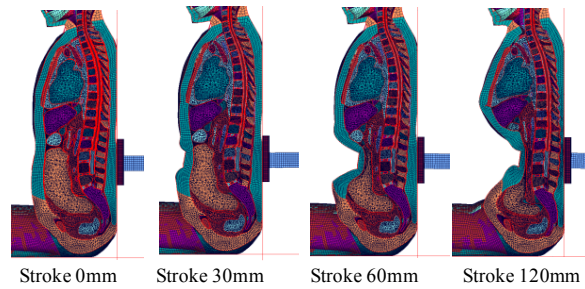


Figure 24. Behavior in abdominal belt test.

Figure 25 compares the deformation of the horizontal section of the abdomen at the height of the belt in its initial state and at a belt deflection of 120 mm. The abdominal sections are shown from the superior view and include the spine, the small and large intestines, the visceral fat near these organs, and the musculature at the posterior portion of the torso. Over the period of time from the initial to the final states, the belt becomes wrapped around the anterior half of the abdomen. The sectional deformation at an abdominal deflection of 120 mm shows that the anterior portion of the abdomen was deformed into a rounded state and the internal portions were compressed toward the spine. The posterior portion was flattened in accordance with the rigid plate. Unlike the impactor case, the body did not elongate in the lateral direction in accordance with AP direction compression. Mostly the small intestine was compressed in the AP direction between the subcutaneous tissue at the anterior surface of the abdomen and the spine. The large intestine was deformed between the subcutaneous tissue at the anterior surface of the abdomen and the musculature at the posterior portion of the torso.

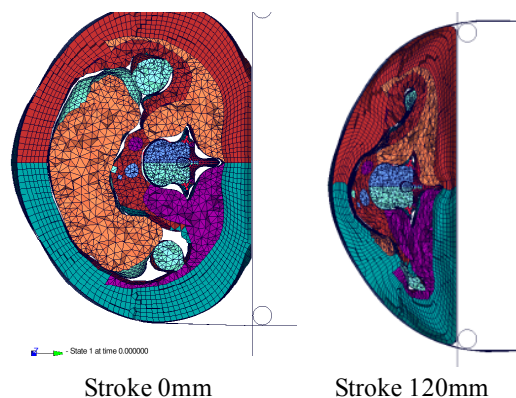


Figure 25. Sectional deformation of abdomen (at height of belt).

Figure 26 shows the time history curves of belt force with respect to abdominal deflection. The grey lines show the force corridor calculated from the PMHS abdominal response, and the black line shows the

response of the FE model. Belt force at a stroke of 20 mm was between 7.5 and 10 kN with the PMHS and 8.0 kN with the FE model. In addition, at a stroke of 75 mm, the force was between 0.4 and 8.0 kN with the PMHS and 5.3 kN with the FE model.

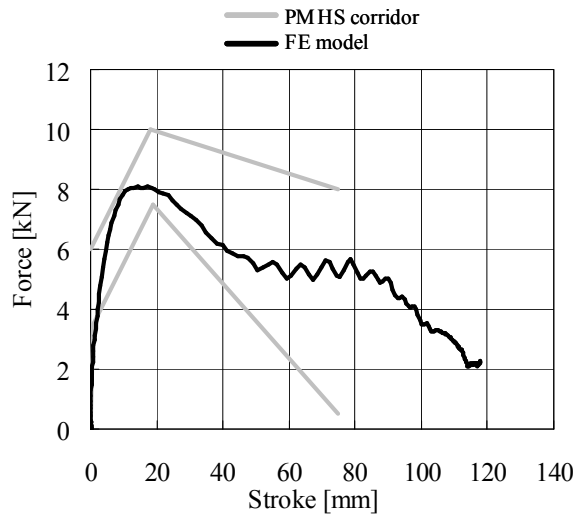


Figure 26. Abdominal belt test F-s.

Foster et al. (2006) tested four PMHS at belt pulling velocities between 6.9 and 13.3 m/s, of which three suffered organ injury. These injuries were to the liver, spleen, and kidneys, but all three injured PMHS were found to have sustained liver laceration. The case used for model verification did not suffer organ injury. Figure 27 shows the strain distribution in the abdominal organs of the FE model. Although the small intestine was compressed by 90% in the AP direction, the maximum strain in the small and large intestines did not exceed the reference value of 1.2. Strain in the intestines exceeded 0.3 close to the 10th rib on the right side, but no other organ exceeded its reference value for strain. These results indicate that the FE model successfully simulated the organ injury conditions of the PMHS for liver injury after abdominal compression. The FE model did not predict injury to any other organ. Its predictive accuracy cannot be discussed for the other organs because the injury results in the PMHS tests varied among the cases.

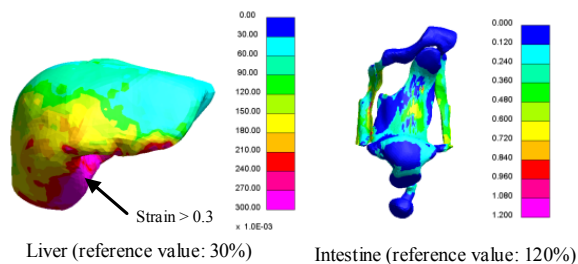


Figure 27. Strain distribution in abdominal organs.

Verification of Extremity Model

Static Bending Response of Humerus - Figure 28 shows the static 3-point bending test performed on the humerus by Kemper et al. (2005). In this test, the humerus was removed from the PMHS, both ends inserted into cylindrical aluminum jigs, and fixed using a hardened resin. One of the jigs was supported using a pin joint allowing rotation in the bending direction only, and the other was supported using a roller allowing the same rotation and displacement in the axial direction of the bone. The center of the humerus was then loaded using an impactor (diameter: 20 mm) at a velocity of 10 mm/s. The test was performed on three humerus bones, and the reaction force with respect to the impactor displacement was recorded. The FE model omitted the jigs and expressed the fixed portions using rigid elements. Nodes were set at the positions equivalent to the jig rotation centers, and defined with conditions for pin and roller support. Forceful displacement was applied by a model impactor on to the model humerus. The displacement of the impactor was output as model node displacement and the reaction force was output as the contact force with the humerus.

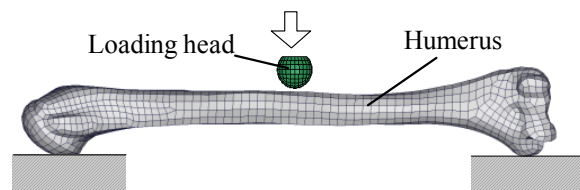


Figure 28. Static 3-point bending of humerus.

Figure 29 compares the force-displacement curves obtained in the three tests with that calculated by the FE model. The reaction force at a displacement of 5 mm was between 1.5 to 3.7 kN with the PMHS and 2.3 kN with the FE model. Additionally, the reaction force at a displacement of 10 mm was between 2.9 to 4.1 kN with the PMHS and 4.2 kN with the FE model. Although the reaction force of the FE model slightly exceeded that of the PMHS range at 10 mm, the curve history to that point fitted within the PMHS reaction force corridor.

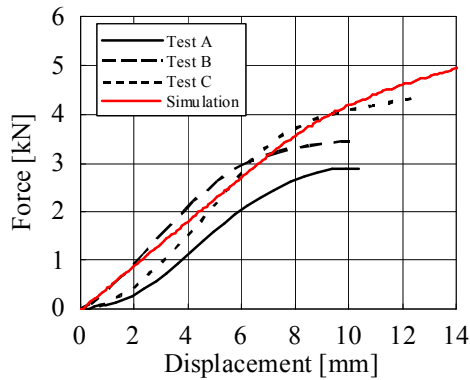


Figure 29. Relationship between impactor displacement and reaction force.

Dynamic Compression Response of Humerus

- Figure 30 shows the dynamic test performed on the humerus by Kemper et al. (2005). In this test, the humerus was extracted from the PMHS including the flesh. The humerus was placed on a circular table with a diameter of 152 mm, and compressed by a circular impactor of the same dimensions applied in the downward direction at a velocity of 4 m/s. The test was performed on two humerus bones and the compressive displacement and compressive force were recorded. The same portion was extracted for the FE model, and placed between models of the circular jigs. The lower jig was fixed in space while the upper jig applied forcible displacement to compress the humerus model. The compressive displacement was output as displacement of the nodes in the upper jig, and the compressive force was output as the contact force between the humerus and the jigs.

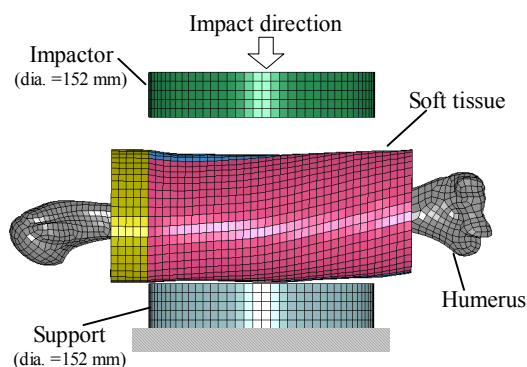


Figure 30. Humerus dynamic compression test.

Figure 31 compares the force-displacement curve obtained in the two tests with that calculated by the FE model. The force at a displacement of 15 mm was between 2 to 4 kN with the PMHS, and 2.5 kN with the FE model. Additionally, the force at a displacement of 25 mm was between 5 to 12 kN with

the PMHS and 6.2 kN with the FE model. The force curve of the FE model was within the force range of the PMHS.

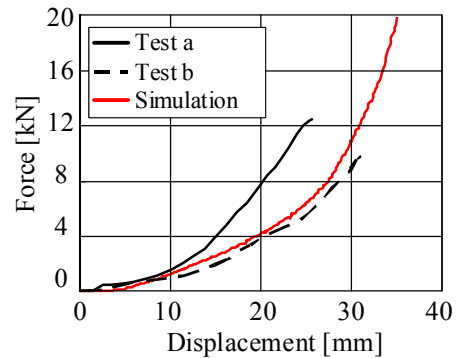


Figure 31. Relationship between impactor displacement and reaction force.

Static Bending Response of Femur

- Figure 32 shows the static bending test performed on the femur by Yamada et al. (1970). In this test, the femur was removed from the PMHS, and both ends supported in a rotatable state. An impactor (diameter: 20 mm) was used to apply force at a velocity of 20 mm/s to the center of the femur. In the FE model, the same portions were also extracted and supported in a rotatable state at both ends. Forcible displacement was applied to the center of the femur in a manner equivalent to the test by a model of a rigid rod impactor. The displacement of the impactor was output as model node displacement and the reaction force was output as the contact force with the femur.

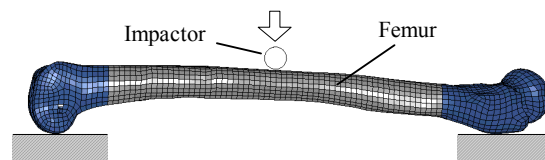


Figure 32. Static 3-point bending of femur.

Figure 33 compares the force-displacement curve obtained in the test with that calculated by the FE model. There is only one set of comparison data. The force at a displacement of 5 mm was 1.7 kN with the PMHS and 1.4 kN with the FE model. Additionally, the force at a displacement of 10 mm was 2.5 with the PMHS and 2.4 kN with the FE model. The force curve of the FE model was close to that of the PMHS.

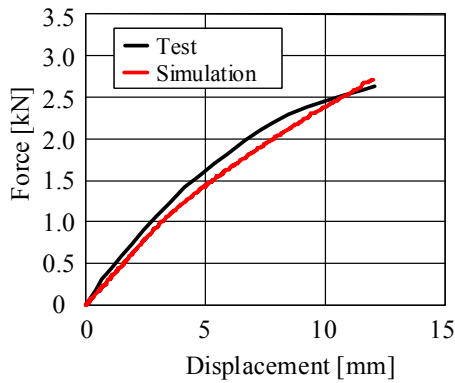


Figure 33. Relationship between impactor displacement and reaction force.

Impact Response of Knee - Figure 34 shows the impact test performed on the knee by Kajzer et al. (1997). This test used the lower extremity of a PMHS. The femur was fixed and an impactor (mass: 6.25 kg) was applied to the knee from the side at a velocity of 40 km/h, while force of 400 K was applied from under the foot. The diameter of the impactor was 100 mm, and a pad (thickness: 50 mm) was attached to its front surface. The test was performed on two lower extremity specimens, and the acceleration on impact was recorded by an accelerometer provided at the superior portion of the tibia. The same portion was extracted for the FE model, which also simulated the tibia support initial force under the foot. An impactor model was created and applied to the side of the knee at a velocity of 40 km/h. The acceleration was output from a node at an equivalent position to the accelerometer in the PMHS test.

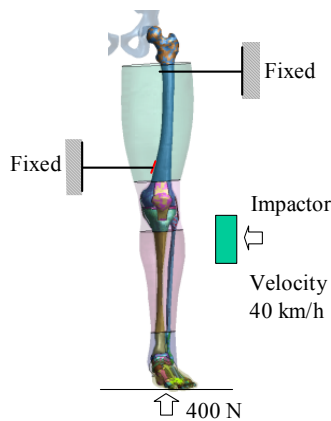


Figure 34. Knee impact test.

Figure 35 compares the acceleration time history obtained in the two tests with the acceleration curve calculated by the FE model. In all cases, acceleration peaked at approximately 4 ms after the impact, and then decreased. Peak acceleration with the PMHS was between 930 and 1020 m/s^2 , and 1060 m/s^2 with

the FE model. With the FE model, acceleration declined gradually immediately after the peak, but it re-produced the plateau in the acceleration curve at approximately 10 ms. Overall, the acceleration response of the FE model was higher than that of the PMHS, but their acceleration waveforms correlated well.

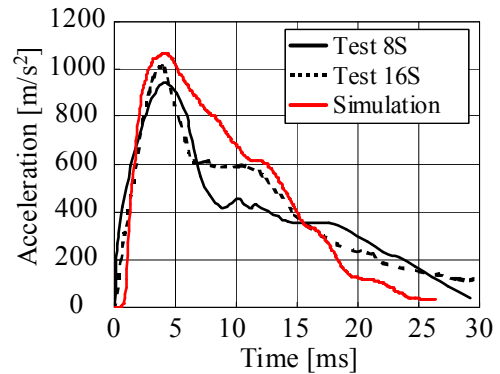


Figure 35. Impactor acceleration time history.

DISCUSSION

The predicted mechanical response of the thorax, abdomen, and extremities in the FE model correlated well with PMHS test data under the equivalent conditions. Although there is only limited data available to compare abdominal organ injury, the injuries predicted by the FE model based on assumed reference values correlated well with the PMHS test results. It is difficult to observe organ behavior during impact in PMHS tests, but FE model simulations visualized the internal behavior. Additionally, PMHS tests require precise techniques for attaching sensors such as load cells and potentiometers. FE models are capable of outputting force and displacement at any point of interest. It was useful to consider the mechanism of injuries incurred by thoracic and abdominal organs by analyzing the results of the model validation simulations, as follows.

Injury Mechanism of Thoracic Organs

According to the test results of Kroell et al. (1971) used to verify thoracic impactor response, multiple (seven or more) rib fractures occurred in all cases of organ injury. In contrast, in cases without rib fracture, no organ injury occurred. As shown in Figure 10, the anterior surface of the FE model thorax was flattened by the impactor. As a result, the lungs suffered compressive deformation as well as the heart located in the center of the thorax. At a thoracic deflection of approximately 70 mm, the thorax sectional area decreased by a ratio of approximately 21%. Figure 36 shows the time history of thoracic deflection

calculated at the sternum of the FE model overlaid with the time histories of strain in the heart, liver and lung pressure. Thoracic deflection increased immediately after impactor contact and reached a maximum value of 75 mm at approximately 14 ms. However, before that, the sternum and 4th rib fractured at 8 ms (thoracic deflection: 58 mm), and rib fractures occurred in six locations before the maximum thoracic deflection was reached. Strain in the heart and liver both increased in accordance with the thoracic deflection. Since the heart is located in the center of the thorax, it was caught between the sternum and the spine when the thorax was compressed in the AP direction. As a result, strain in the heart increased at the same time as the thoracic deflection. The left end of the liver was elongated up to a position close to the center of the body, but this area is located inferior to the bottom of the sternum. Under these conditions, since the liver was located slightly inferior to the impactor contact point, the increase in strain occurred a little later than for the heart. Therefore, it is considered that the organ strain timing differed depending on the position of the organ with respect to the pressure application area. The pressure in the lungs, which along with the heart were also immediately below the impactor, increased drastically from approximately 8 ms. This indicates that lung deformation was advanced by the start of the sternum and rib fractures.

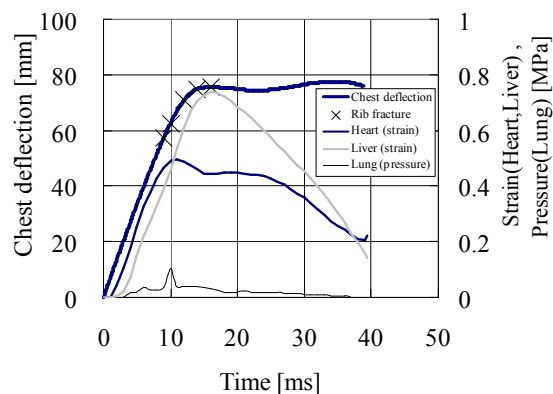


Figure 36. Thoracic deflection and organ force on impactor contact.

In contrast, although the heart was also compressed in the AP direction under the belt compression conditions in the same way as with the impactor contact, compressive deformation of the lungs was relatively small (Figure 16). In these sections, the belt mostly loaded the sternum. The surrounding ribs were not deformed a great deal, but were bent slightly inward dragged by the sternum. At a thoracic deflection of approximately 70 mm, the thorax sectional area decreased by a ratio of approximately 15%. Figure 37 shows the time history of thoracic

deflection calculated by the FE model overlaid with the time histories of strain in the heart and liver and lung pressure. Under these conditions, strain in the heart and liver and lung pressure all increased in accordance with the increase in thoracic deflection. The sections in Figure 16 show the belt was positioned at the sternum, but multiple organs were compressed since the belt was actually placed diagonally across the anterior surface of the thorax. However, it is assumed that the deformation of the compressed organs was low because the ratio of sectional area decrease was less than with the impactor in these sections. In fact, the strain in the heart and liver shown in Figure 37 was smaller than at the same thoracic deflection in Figure 36. Strain in the liver was smaller because it was outside the area compressed by the belt. The amount of compressive deformation of these organs may have been small since the belt may have loaded multiple organs simultaneously. Deformation had a higher trend for the organs underneath the contact surface of the impactor. In other words, the thoracic organ injury risk may also be affected by the compression area and not only the amount of thoracic deflection. Since the study performed by Cesari et al. (1990) does not describe organ injury, the validity of the organ injury predictions under belt loading using the FE model needs to be verified in future study. The liver is located in the abdominal area, but it is covered by the inferior ribs. In the thoracic impactor test, strain was generated in the superior part of the liver by deformation of the right ribs. Although the liver was located away from the belt path in the reference test case, it would be compressed if the belt were worn over the other shoulder.

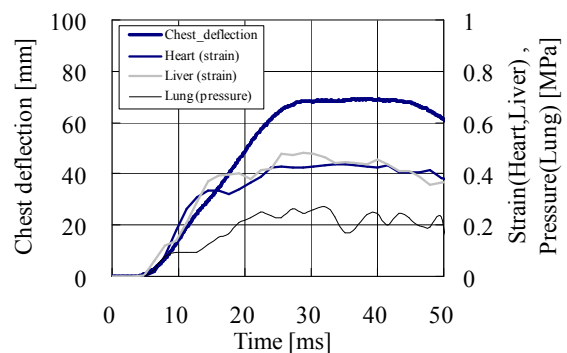


Figure 37. Thoracic deflection and organ force on belt compression.

Injury Mechanism of Abdominal Organs

A similar trend was observed for the abdomen. However, no large differences were found in the size of the abdomen compression area between the impactor and belt test. Comparing the abdominal

deformation in the sections in Figures 20 and 25, the former shows that the impactor flattened the anterior surface of the abdomen, whereas in the latter, the belt became wrapped around the anterior half of the abdomen and caused deformation by restraining the body toward the center. In other words, with impactor contact, large compression occurred above the impactor center, but the belt force applied large compression over the whole range of contact. At an abdominal deflection of approximately 60 mm, the abdominal sectional area decreased by approximately 13% with the impactor, and approximately 39% with the belt. That is, organ deformation and movement were larger under the belt conditions. Figures 38 and 39 show the time history of abdominal deflection calculated by the FE model overlaid with the time histories of strain for the small and large intestines and the liver, under both the abdominal impactor and belt compression conditions. Strain was output at the elements of the small and large intestines positioned at the height of the impactor. Elements close to the impactor were selected for the liver. In both cases, strain of the small intestine increased at the same time as the increase in abdominal deflection. Strain in the liver began to increase as compressive deformation of the abdomen progressed to a certain level, and increased again after abdominal deflection and strain in the small intestine peaked. This is probably because a portion of the liver is connected with the diaphragm, which causes compressive or tensile deformation when pulled by other organs under abdominal compression. The strain value in the liver was smaller than that in the small intestine. It should be noted, however, that the reference strain value for the liver is relatively small. In both cases, strain in the large intestine increased temporarily when abdominal compression reached a certain point, but eventually decreased. Although the large intestine is connected to the peritoneum, its long path gives it a larger tolerance for movement than organs such as the liver.

Limitations and Suggestion for Future Work

The human FE model developed in this research demonstrated a good correlation with the mechanical response of PMHS tests selected from the literature. However, there are limitations in the selected force conditions and cases that be used for comparison. Therefore, the validation results cannot confirm the validity of the model under various force conditions. Further research is needed for human injury prediction in vehicle collisions using this model.

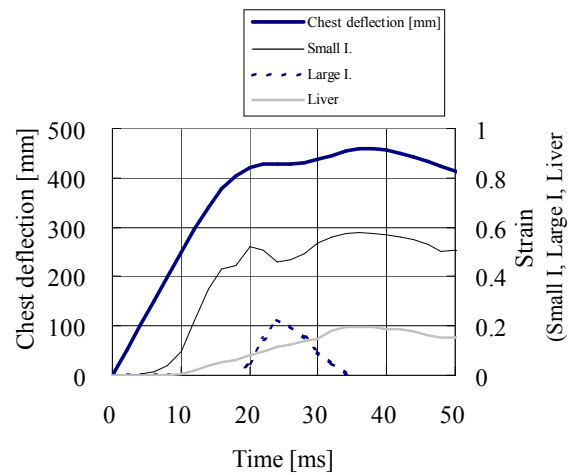


Figure 38. Abdominal deflection and organ force on impactor contact.

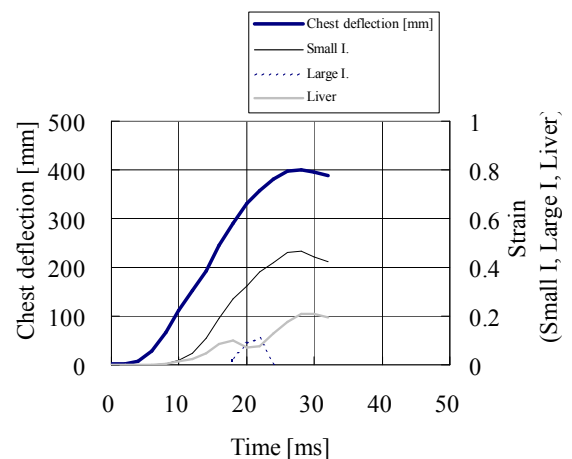


Figure 39. Abdominal deflection and organ force on belt compression.

CONCLUSION

A precise FE model of a torso was developed based on internal geometrical data digitized using high-resolution CT scans. The model was generated taking into account the properties of each organ and their connections with neighboring tissues. FE models were also created for the extremities with the same precision as the torso based on commercially available geometrical databases. THUMS ver.3.0 was used for the head model. These models were combined to complete a whole human body FE model (THUMS ver.4.0) comprising approximately 2 million elements simulating an adult male of average physique. The validity of the mechanical response of the developed human FE model was verified by comparison with PMHS impact test data. FE models simulated impactor and belt compression tests on the thorax and abdomen, 3-point bending tests on the extremities, and impactor tests on the knees to verify

correlation with PMHS force response. The mechanism of organ injuries in the thorax and abdomen was also discussed based on the validation results. Strain in heart and lung pressure increased in accordance with thoracic deflection, but the magnitude of them was affected by the compression area of the loading device. Strain in the small intestine increased in accordance with abdominal deflection, while strain in the liver increased locally as compressive deformation of the abdominal progressed. The absolute values for pressure and strain indicated by the FE model require further verification, but the developed FE model was shown to be useful for predicting trends of organ injuries in vehicle collisions.

ACKNOWLEDGMENTS

The human body geometry data was obtained with a high resolution CT-scan system developed by the University of Michigan. The authors wish to thank Dr. Stewart Wang for providing the digitized geometry data. Many of the techniques used for modeling were based on experience from using the THUMS model. THUMS was developed in collaboration with Toyota Central R & D Labs., Inc. The authors would also like to thank Toyota Technical Development Corporation for its assistance in the modeling and simulation work.

REFERENCES

- [1] McHenry, R. R. 1963. "Analysis of the dynamic of automobile passenger restraint systems." Proc. 7th Stapp Car Crash Conference, pp. 207-249.
- [2] Choi, H. Y., Lee, I. H. and Haug, E. 1999. "Advanced finite element modeling of the human body for occupant safety; H-Model for the next millennium." Proceeding of 5th HanPam, Seoul, Korea.
- [3]Iwamoto, M.; Kisanuki, Y.; Watanabe, I.; Furusu, K.; Miki, K.; Hasegawa, J. 2002. "Development of a finite element model of the total human model for safety (THUMS) and application to injury reconstruction." Proc. International Conference on the Biomechanics of Impacts, pp. 31-42.
- [4] Vezin, P., Verriest, J. P. 2005. "Development of a Set of Numerical Human Models for Safety." Proc. 19th ESV Conference, 05-0163.
- [5] Ruan, J. S., El-Jawahri, R., Chai, L., Barbat, S., Prasad, P. 2003. "Prediction and Analysis of Human Thoracic Impact Response and Injuries in Cadaver Impacts using a full human Body Finite Element Model." Stapp Car Crash Journal, 47:299-321.

[6] Kitagawa, Y., Hasegawa, J., Yasuki, T. 2005. "A Study of Knee Joint Kinematics and Mechanics using a Human FE Model." Stapp Car Crash Journal, 49:117-131.

[7] Hayashi, S., Yasuki, T., Yamamae, Y., Takahira, Y. 2006. "A Study of Side Airbag Effectiveness in Reducing Chest Injury in Car to Car Side Impacts Using a Human FE Model." Proc. 2006 International Research Council on the Biomechanics of Impacts (IRCOBI), pp. 397-400.

[8] Kuwahara, M., Yasuki, T., Kitagawa, Y., Hayashi, S., Masuda, T. 2008. "A Study of SRS Side Airbag Performance in Chest Protection in a Pole Side Impact using a Human FE Model." Proc. 2008 FISITA, F2008-08-015.

[9] Kitagawa, Y., T. Yasuki and J. Hasegawa. 2006. "A Study of Cervical Spine Kinematics and Joint Capsule Strain in Rear Impacts Using a Human FE Model." Stapp Car Crash Journal 50: 545-566.

[10] Kitagawa, Y., T. Yasuki and J. Hasegawa. 2007. "Consideration of Possible Indicators for Whiplash Injury Assessment and Examination of Seat Design Parameters using Human FE Model." Proc. 20th ESV Conference, 07-0093.

[11] Kitagawa, Y., Yasuki, T., Hasegawa, J. 2008. "Research Study on Whiplash Injury Lessening with Active Head Restraint using a Human FE Model." Proc. 2008 International Research Council on the Biomechanics of Impacts (IRCOBI), pp. 381-396.

[12] Yasuki, T. 2005. "A Survey on the Biofidelity of the Knee Bending Angle of the TRL Lower Leg Impactor." Proc. 19th ESV Conference, 05-0101.

[13] Tamura, A., Nakahira, Y., Iwamoto, M., Watanabe, I., Miki, K., Hayashi, S., Yasuki, T. 2006. "The Influence of the Traction Force Due to Inertia of the Brain Mass on Traumatic Brain Injury during SUV-to-Pedestrian Impact." International Research Council on the Biomechanics of Impacts (IRCOBI), pp. 361-364.

[14] Hayashi, S., Yasuki, T., Kitagawa, Y. 2008. "Occupant Kinematics and Estimated Effectiveness of Side Airbags in Pole Side Impacts Using a Human FE Model with Internal Organs." Stapp Car Crash Journal, 52: 363-377.

[15] Yamada, H. 1970. "Strength of Biological Materials." FG. Eevan, Ed., The Williams & Wilkins Company, Baltimore.

- [16] Abe, H., Hayashi, K., Sato, M. 1996. "Data Book on Mechanical Properties of Living Cells, Tissues and Organs." Springer-Verlag Tokyo.
- [17] Kimpara, H., Nakahira, Y., Iwamoto, M., Miki, K., Ichihara, K., Kawano, S., Taguchi, T. 2006. "Investigation of Anteroposterior Head-Neck Responses during Severe Frontal Impact Using a Brain-Spinal Cord Complex FE Model." *Stapp Car Crash Journal*, Vol.50, pp. 27-51.
- [18] Shah, J.S., Yang, K.H., Hardy, W.N., Wang, H.K. and King, A.I. 2001. "Development of a computer model to predict aortic rupture due to impact loading." *Stapp Car Crash Journal*, Vol.45, pp.161-182.
- [19] Lee, J.B., and Yang, K.H., 2001. "Development of a finite element model of the human abdomen." *Stapp Car Crash Journal*, Vol.45, pp. 79-100
- [20] Kroell, C., Schneider, D., Nahum, A. 1971. "Impact Tolerance and Response of the Human Thorax." *Proc. 15th Stapp Car Crash Conference*, pp. 84-134.
- [21] Kroell, C., Schneider, D., Nahum, A. 1974. "Impact Tolerance and Response of the Human Thorax II." *Proc. 18th Stapp Car Crash Conference*, pp. 383-457.
- [22] Cesari, D., Bouquet, R. 1990. "Behaviour of Human Surrogates Thorax under Belt Loading." SAE902310.
- [23] Cavanaugh, J., Nyquist, G., Goldberg, S., King, A. 1986. "Lower Abdominal Tolerance and Response". SAE861878.
- [24] Foster, C., Hardy, W., Yang, K., King, A., Hashimoto, S. 2006. "High-Speed Seatbelt Pretensioner Loading of the Abdomen." *Stapp Car Crash Journal*, Vol.50, pp. 27-51.
- [25] Kemper, A., Duma, S., Matsuoka, F., Masuda, M. 2005. "Biofidelity of the SID-IIs and a Modified SID-IIs Upper Extremity: Biomechanical Properties of the Human Humerus." *Proc. 19th ESV Conference*, 05-0123
- [24] Kemper, A., McNally, C., Kennedy, E., Rath, A., Manoogian, S., Stitzel, J., and Duma, S. 2005. "Material Properties of Human Rib Cortical Bone from Dynamic Tension Coupon Testing." *Stapp Car Crash Journal*, Vol.49, pp. 199-230.
- [25] Karl, E.S., Wilbur, P.M, Jr., Charles, C.C., Averill, A.L. 1958. "Mechanisms in Development of Interstitial Emphysema and Air Embolism on Decompression From Depth." *Journal of Applied Physiology*, Vol.13, pp. 15-29.